Journal of Materials Chemistry A

Screening binary alloys for electrochemical CO2 reduction towards multi-carbon products

Journal:	*Journal of Materials Chemistry A*
Manuscript ID	TA-ART-04-2022-002749.R1
Article Type:	Paper
Date Submitted by the Author:	13-Jun-2022
Complete List of Authors:	Li, Jiang; Stanford University, School of Chemical Engineering Halldin Stenlid, Joakim; Stockholm University Faculty of Natural Sciences, Physics Tang, Michael; Stanford University, Department of Materials Science Engineering; SLAC National Accelerator Laboratory, SUNCAT Center for Interface Science and Catalysis Peng, Hong-Jie; Tsinghua Univeristy, Department of Chemical Enginnering Abild-Pedersen, Frank; Stanford Linear Accelerator Center, SUNCAT

Screening binary alloys for electrochemical CO_2 reduction towards multi-carbon products

Jiang Li[a,b], Joakim Halldin Stenlid[a,b], Michael T. Tang[a,b], Hongjie Peng[a,b], Frank Abild-Pedersen[b,*]

[a]*SUNCAT Center for Interface Science and Catalysis, Department of Chemical Engineering, Stanford University, Stanford, CA 94305, USA*

[b]*SUNCAT Center for Interface Science and Catalysis, SLAC National Accelerator Laboratory, 2575 Sand Hill Road, Menlo Park, California 94025, United States*

**Corresponding author: abild@slac.stanford.edu*

Abstract

Electrochemical reduction of CO_2 (eCO_2R) to high-value chemicals presents an attractive approach for utilizing CO_2. Copper (Cu) is presently the only electrocatalyst that fulfills this purpose with notable activity, but selectivity remains a problem. To identify catalysts for eCO_2R with high selectivity towards multicarbon (C_{2+}) products, we explore binary systems comprised of strongly and weakly CO binding metals alloyed with Cu, Fe, Co, Ni, and Pd. A total number of 142 alloys with two commonly studied configurations, $L1_2$ and $L1_0$, are simulated with density functional theory (DFT). We leverage recent progress in the atomistic understanding of the eCO_2R mechanism and use the binding energies of CO* and C* as descriptors when screening for C_{2+} selectivity. We evaluate the stability of the binary alloys by analyzing the formation energy of the clean alloy surfaces. Our theoretical screening identifies about 16 Cu-based alloys and 18 non-Cu based alloys with optimal C_{2+} selective properties for eCO_2R. For the non-Cu based binary alloys, the *p*-block elements play an important role in tuning the C* and CO* adsorption energies. In terms of stability, most of the Cu-based systems alloyed with metals that exhibit strong CO* binding are unstable. Ni-based alloys are more stable than the Co-based alloys followed by the Fe-based alloys, and all the Pd-based alloys are stable. In general, the $L1_0$ structural Fe, Co, Ni, and Pd-based alloys are more stable than the corresponding $L1_2$ alloys. Our approach identifies materials known to have good C_{2+} selectivity, but it also proposes several other promising materials that have not previously been tested for eCO_2R.

Keywords: Density functional theory; CO_2 electrochemical reduction; Binary alloys; C_2 product selectivity; Alloy stability.

1. Introduction

Global chemical and energy industries rely heavily on fossil fuel feedstock. At the same time, substantial emission of greenhouse gases such as carbon dioxide (CO_2) leads to elevated temperatures that alter the Earth's climate.[1] Technologies for mitigating CO_2 emission via capturing, sequestration, and/or conversion in an electrochemical, photocatalytic, or thermochemical manner, have been widely studied.[2-7] Among these approaches, electrochemical CO_2 reduction (eCO_2R) has risen as an elegant and plausible route for conversion of CO_2 into valuable chemicals and fuels that can be powered by electricity from clean and renewable (e.g., solar, wind, hydroelectric, nuclear, and geothermal) energy resources.[8-12] The eCO_2R has a complex reaction network with a variety of possible reduced products, ranging from two-electron products (CO or formate) to hydrocarbons and oxygenates such as methane, ethylene, ethanol, acetic acid, and n-propanol.[13-14] Comparatively, highly reduced multi-carbon (C_{2+}) species are of greater value as building blocks in chemical synthesis and the C_{2+} oxygenates are more suitable for energy storage and transportation.[15-16] However, tuning the kinetics of eCO_2R is a challenging endeavor and the lack of sufficiently active and selective electrocatalysts presents a roadblock for industries to take on the eCO_2R.[17-18]

Copper (Cu) is currently the only metal that produces high-value C_{2+} products at an acceptable rate; however, its selectivity is still far from satisfactory.[19] The unique ability of Cu to form C_{2+} products has been attributed to its moderate binding energy of CO and other intermediates, whereas the selectivity issue is related to the relatively flat reaction landscape towards different types of products highlighting the need to fine-tune the catalysts' properties.[20-21] In this respect, exploring electrocatalyst structures with more than one element is a promising approach towards enhanced selectivity in eCO_2R by offering tunable control over structure, morphology, and composition.[22] However, the approach also leads to an amplified combinational task for identifying the ideal catalysts.

Recent advances in high-throughput experimental synthesis and computational screening based on density functional theory (DFT) calculations have immensely boosted the discovery of eCO_2R electrocatalysts. Experimentally, Grote *et al.*[23] developed a composition screening technique that synthesizes thin film samples with a co-sputtering approach and performs electrochemical measurement through a scanning flow cell coupled to an online electrochemical mass spectrometer (SFC-OLEMS). They investigated the Cu-Co system in the entire

compositional range and revealed that there is a shift in selectivity toward C_2 products for low Co content (in the range of 5-15 atomic percentage) and that higher Co concentration promotes the hydrogen evolution reaction (HER) over the eCO_2R. Berlinguette and coworkers[24] developed a high-throughput synthesis technique by reducing films formed by near-infrared driven decomposition (NIRDD) of metal salts. They studied a series of binary metallic electrocatalysts and found that Indium (In) efficiently suppresses HER for all the Fe-, Co-, Ni-, and Cu-based alloys and that the Cu(80%)-In alloy exhibits excellent CO selectivity with a Faradaic efficiency (FE) greater than 80%. In terms of the DFT-based screening work, the approaches developed by Nørskov and co-workers [25-27] are widely used in which reactivity trends are estimated from adsorption energies of intermediates evaluated on pure metals or on multi-metallic alloys, and has made significant contribution to the theoretical screening of electrocatalysts for eCO_2R. Bagger *et al.*[28-29] carried out both experimental and theoretical studies in classifying metallic electrocatalysts and proposed that four non-coupled binding energies of intermediates (H*, COOH*, CO*, and CH_3O*, where * indicates the adsorbed state of the intermediate) can be used to group and explain products distributions in eCO_2R. Zhi *et al.*[30] applied DFT calculations to study a series of Cu-based single atom alloys (M@Cu, M = Co, Ni, Ru, Rh, Ir, Pt, Pd, Au, Ag, Zn, In, Sn) and revealed that the hydrogen and oxygen affinities to M (M-H and M-O) are effective descriptors for eCO_2R selectivity and therefore provides a rational approach in the design of highly selective Cu-based alloys. Zhao *et al.*[31] performed a computational screening of Ni-based near-surface-alloys (NSAs) with a total of 27 alloying elements M (M = 3*d*, 4*d*, and 5*d* transition metals). The introduction of a monolayer of M either to the surface layer or to the subsurface layer identified Ni-Ti and Cu-Ni NSAs as catalysts with excellent formic acid selectivity during eCO_2R. The Xin group[32] presented a machine-learning-augmented chemisorption model that enabled prediction of the complex and nonlinear interactions of adsorbates with multi-metallic alloy surfaces with errors around 0.1 eV, which greatly facilitates the theoretical high-throughput screening of alloys as eCO_2R electrocatalysts. They found a few promising (100)-terminated Cu-based alloys with high efficiency and selectivity for eCO_2R towards C_{2+} species and revealed that the *d*-band characteristics and local electronegativity play significant roles in CO binding on metal surfaces. Tran and Ulissi[33] developed an automated screening approach that applies machine learning to guide DFT calculations. They screened various alloys of 31 different elements and identified 131 candidate surfaces across 54 binary

alloys with optimal (-0.67 eV) CO binding energy for eCO_2R. Most of the promising candidates identified were the strong-weak elemental pairings with combinations of strong CO binding elements (e.g., Pd, Pt, Ni, Os) with weak CO binding elements (e.g., Al, Sn, Ga, Sb).

Mechanistically, multiple reaction pathways are known to be of importance in eCO_2R with the dominant mechanism varying with, e.g., potential and pH. Among the pathways leading to C-C bond formation, CO-CO dimerization has been identified as the most favorable at low overpotentials and alkaline conditions.[16] Therefore, this pathway has been the main focus of previous screening studies towards C_{2+} selective catalysts.[16, 30-33] Recently, we reexamined the mechanistic pathways of eCO_2R in detail accounting explicitly for pH, potential, and electric field effects;[34] the most critical steps towards C_{2+} products at different conditions could be identified, nuancing the atomic scale understanding, and providing a basis for an intelligible descriptor-based protocol for screening C_{2+} selective electrocatalysts. In particular, it was found that atomic carbon, C*, is a key intermediate for the bifurcation into either C_1 (methane) or C_{2+} products through protonation of or CO-coupling to C*, respectively. This singled out C* and CO* adsorption energies onto the catalysts surface as two decisive descriptors for rationalization of C_{2+} selectivity. With some variations with applied potential, the most active eCO_2R surfaces were identified to have moderate (0.0 to -0.6 eV) CO* binding energies and slightly endergonic (0.5 to 1.5 eV) C* binding energies.

In this work, we leverage the recent mechanistic insights and carry out a computational screening of Cu-based binary alloys composed of Cu with strong CO binding metals (Fe, Co, Ni, Pd, Pt, Mo, Ru, Rh, W, Re, Os, Ir) or with weak CO binding metals (Zn, Ag, Au, Al, Ga, In, Si, Ge, Sn, Pb, As, Sb, Bi). We also investigate non-Cu based binary alloys with combinations of strong and weak binding metals. We consider the two common $L1_2$ and $L1_0$ alloying configurations.[35-37]Adsorption energies of C* and CO* on a total number of 142 binary alloys are calculated with DFT and these two descriptors are used to screen for C_{2+} selective alloys. In addition, the stability of the binary alloys is evaluated via the formation energies of the binary alloy surfaces. Our theoretical screening not only identify several Cu-based alloys with ideal properties, some of them reported experimentally and some yet to be tested, but also suggests a few promising Ni-, Co-, Fe-, and Pd-based binary alloys. The selectivity and stability trends of the binary alloys as revealed in this work provides rational guidance in designing highly C_{2+}

selective and stable alloys for eCO_2R including other structures and compositions, as well as multicomponent systems ranging beyond bi-metallics.

2. Calculation Details

First-principle calculations were carried out with a periodic plane-wave implementation using the QUANTUM ESPRESSO code,[38] interfaced with the Atomistic Simulation Environment (ASE).[39] The BEEF-vdW functional was applied, which provides a reasonable description of van der Waals forces while maintaining an accurate prediction of chemisorption energies.[40] Plane-wave and density cutoffs were 500 eV and 5000 eV, respectively, with a Fermi-level smearing width of 0.1 eV. The bulk structures of pure metals and binary alloys were optimized using the variable-cell relax (vc-relax) approach in QUANTUM ESPRESSO. The adsorption energies on (100) and (110) surfaces of *fcc* transition metals were evaluated using four-layer (2 × 2) supercells with the bottom two layers constrained and a vacuum layer of 20 Å. Monkhorst-Pack *k*-point grids[41] of (4 × 4 × 1) and (6 × 4 × 1) were used for (100) and (110) surfaces, respectively. Modified psLib ultrasoft pseudopotentials were chosen.[42] All structures were optimized until the force components were less than 0.05 eV $Å^{-1}$. A dipole correction was applied to decouple the electrostatic interaction between the periodically repeated slabs.[43] For binary alloys, the $L1_2$ and $L1_0$ structures were selected because of the relatively low surface energy.[34] The favorite adsorption sites for CO* and C* were tested. CO* tends to adsorb on the atop site of the stronger CO-binding metal, while C* preferentially adsorbs on the four-fold hollow site. Adsorption energies of CO* on atop sites and C* in four-fold hollow sites on the $L1_2$ (100) and $L1_0$ (110) surfaces were calculated with the above-mentioned settings. An overbinding correction to CO adsorption energies (except CO* on Cu, Ag, and Au) was employed because of generalized gradient approximations (GGA) functionals generally positioning the unfilled $2\pi^*$ orbital at too low energy.[44] The correction is based on the vibrational frequency of the internal CO stretch mode of *CO, relative to the frequency in vacuum.[45] Vibrations were treated in the harmonic oscillator approximation. Details of Gibbs free energy correction can be found in **Supplementary Note 1**. All the adsorption potentials and free energies on pure metals and binary alloys are provided in the Supporting Information (**SI**) (see **Table S1** and **S2**). All the relaxed structures (bulks and surfaces) and reaction energetics are available in the data repository *Catalysis-Hub*[46] at https://www.catalysis-hub.org/publications/LiScreening2021.

3. Results and Discussions

3.1 Selectivity Map

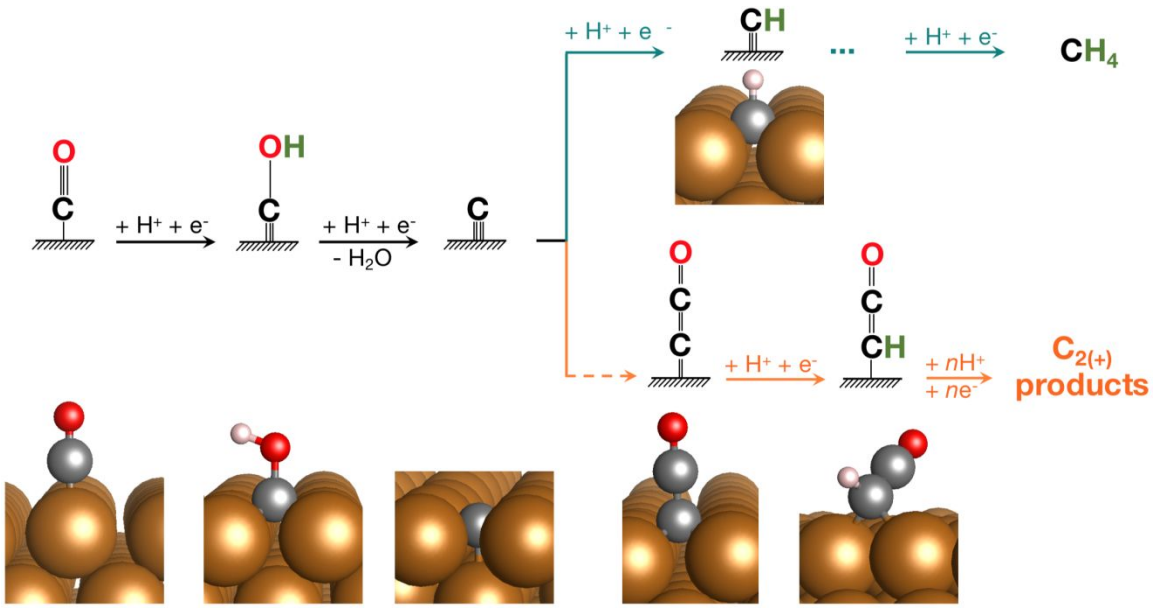

Figure 1 Schematic diagram of the reaction steps beyond CO for pathways toward C_1 (CH_4 as the main product) and $C_{2(+)}$ products.[34, 47] Only the C-CO pathway important for deciding selectivity in $C_{2(+)}$ formation[34] is shown. The atomic structures of the major intermediates are inserted at the bottom.

It has been verified in numerous studies that CO* is a key intermediates in the electrochemical reduction of both CO and CO_2 (hereafter denoted as $eCO_{(2)}R$) leading reduced products beyond two electrons products – i.e., CO(g) and formic acid (HCOOH).[34, 48-49] In our previous work,[34] we present evidence that atomic carbon, C*, plays an equally important role for $C_{2(+)}$ product selectivity at pH < 11 and that this short-lived intermediate can explain the observed surface structure dependence during $CO_{(2)}R$ on Cu. The formation of $C_{2(+)}$ products via the coupling between C* and CO* (C-CO mechanism) is able to rationalize several experimental observations that the CO-dimerization mechanism has failed to explain under neutral pH conditions, particularly for the competition between methane and $C_{(2+)}$ production. For instance, it provides a rationale why 4-fold sites of, e.g., Cu(100) are more $C_{2(+)}$-selective than 3-fold site of, e.g., Cu(111) as the C* binding energy varies significantly between these two types of sites. The fundamental insights developed through the C-CO mechanism has helped us identify the relevant descriptors for the product selectivity and thus paves the way for discovering new $eCO_{(2)}R$ catalysts with high selectivity towards $C_{2(+)}$ products.

Extending from our previous work, where the COH-to-C* pathway is assumed to contribute significantly to C_{2+} product selectivity on Cu(100)-like surfaces at neutral-pH,[34] the rationalization of the C-CO mechanism pathway enable us to employ thermodynamic constraints and scaling relations to screen for binary alloys that have Cu-like CO* and C* binding energetics. **Figure 1**, a schematic diagram showing the important mechanistic steps is given. The key reaction steps that determine the $eCO_{(2)}R$ activity and selectivity are as follows:[34]

(i) $CO^* (\text{or } CO(g) + \ *) + H^+ + e^- \rightarrow COH^* (CO - H \text{ protonation})$

(ii) $CO^* (\text{or } CO(g) + \ *) + 2(H^+ + e^-) \rightarrow C^* + H_2O (C \text{ formation})$

(iii) $CO(g) \ (\text{or } CO^*) + C^* \rightarrow CCO^* \ (C - CO \text{ coupling})$

(iv) $C^* + H^+ + e^- \rightarrow CH^* \ (C - H \text{ protonation})$

Here reactions (i) and (ii) determine the overall rate that explicitly accounts for the shift in the rate-determining step with applied potential, while the competition between (iii) and (iv) determines the selectivity toward C_1 or $C_{2(+)}$ products. We stress that these insights are based on calculations including both solvation, pH, coverage, potential, and field effects.[34]

Assuming that the reaction energies (ΔG_{rxn}) in (i)-(iv) can be adequately described via scaling with the free energies of CO* and C* (G_{CO*} and G_{C*}), we can construct a selectivity map of $CO_{(2)}R$ towards $C_{2(+)}$ products based on the following thermodynamic conditions:[34]

(1) CO* reduction to COH* at an acceptable rate (TOF 1 s^{-1} $site^{-1}$ at 300 K): $\Delta G_{\text{rxn}}^{(\text{i})} < 0.75 \text{ e}V$

(2) CO* reduction to C* is kinetically accessible: $\Delta G_{\text{rxn}}^{(\text{i})} = 0$

(3) C-CO coupling should be more favorable than CO* adsorption: $\Delta G_{\text{rxn}}^{(\text{iii})} < G_{CO^*}$

(4) C-CO coupling should be more favorable than C-H protonation: $\Delta G_{\text{rxn}}^{(\text{iv})} < \Delta G_{\text{rxn}}^{(\text{iii})}$

Depending on the electrochemical conditions, the $C_{2(+)}$ selectivity varies with the applied potentials. At -0.7 V *vs.* RHE (pH7), the overall $C_{2(+)}$ selectivity map for $L1_2$ and $L1_0$ alloys is shown in **Figure 2**. We want to point out that while the G_{CO*} and G_{C*} descriptors are computed at 0.0 V *vs.* RHE, the scaling relations defining the conditions (1)-(4) varies with applied potential giving rise to potential dependent selectivity maps.

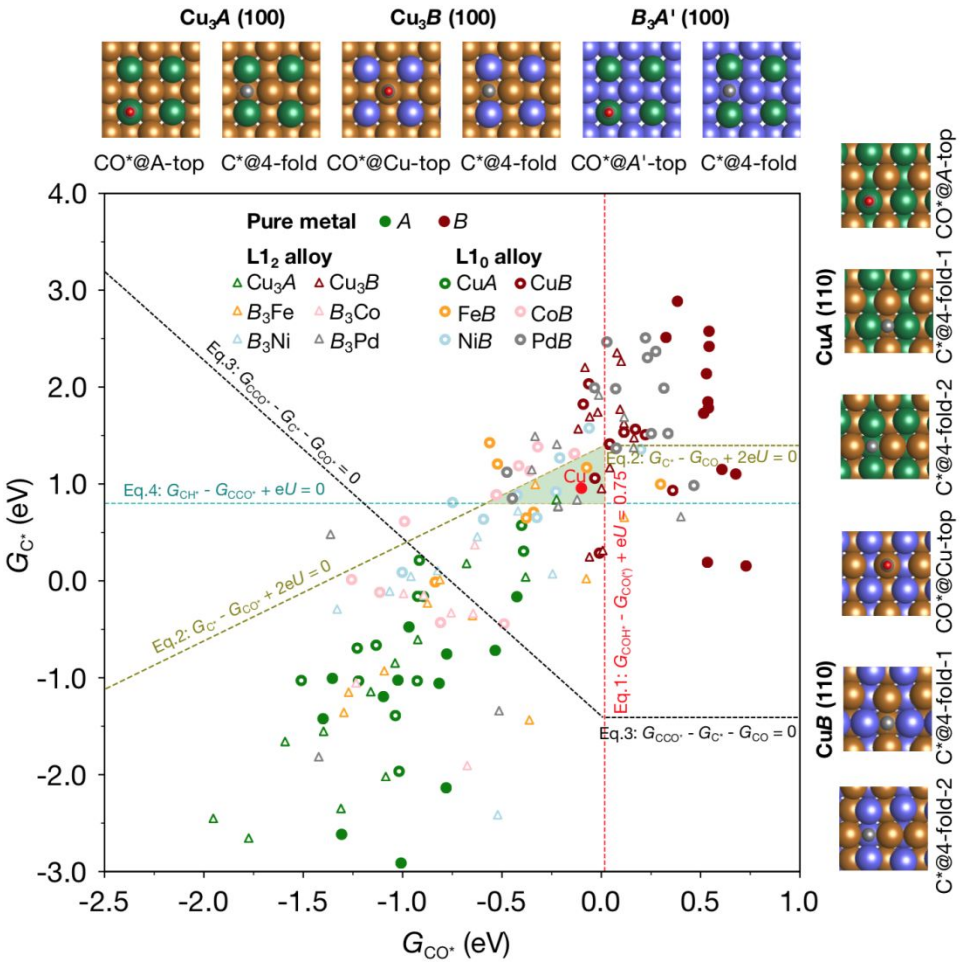

Figure 2 Selectivity map of (100) $L1_2$ and (110) $L1_0$ alloy surfaces at U_{RHE} = -0.7 V (pH7). Details of how to plot the selectivity map were introduced in our previous work.[34] The region with primary selectivity towards C_2-products is highlighted in light green. Solid green dots represent surfaces of pure metal *A*, which are strongly CO binding metals (Fe, Co, Ni, Pd, Pt, Mo, Ru, Rh, W, Re, Os, Ir); solid dark red dots are surfaces of pure metal *B*, which are weakly CO binding metals (Zn, Ag, Au, Al, Ga, In, Si, Ge, Sn, Pb, As, Sb, Bi). The moderate CO binding metal Cu is close to the center of the triangular C_2 selective region. Triangles denote the $L1_2$ binary alloys of Cu_3A (green), Cu_3B (dark red), B_3Fe (orange), B_3Co (pink), B_3Ni (light blue), and B_3Pd (gray). Circles represent the $L1_0$ binary alloys of Cu*A* (green), Cu*B* (dark red), Fe*B* (orange), Co*B* (pink), Ni*B* (light blue), and Pd*B* (gray). Atomic structures (top views) of the adsorption sites of C* (4-fold site) and CO* (top site) are arranged at the top ($L1_2$ alloy) and right side ($L1_0$ alloy) of the figure, where *A*′ denotes the strongly CO binding metals Fe, Co, Ni, and Pd. The structures of $L1_0$ *A*′*B* (110) surfaces are similar to those of the Cu*B* (110) and are therefore not shown in the figure.

In **Figure 2** the selectivity map for $C_{2(+)}$ production on (100) surfaces of A_3B alloys in the $L1_2$ structure and on (110) surfaces of *AB* alloy in the $L1_0$ structure are shown as a function of the adsorption free energies of CO* and C*. For pure metal systems with strong CO binding metals like *A* = (Fe, Co, Ni, Pd, Pt, Mo, Ru, Rh, W, Re, Os, Ir) the points are generally scattered in the bottom part of the figure and for the pure metal systems with weak CO binding metals like *B* = (Zn, Ag, Au, Al, Ga, In, Si, Ge, Sn, Pb, As, Sb, Bi) the points are spread in the region on the

upper right part of the figure. None of these pure metals are particularly $C_{2(+)}$ selective. This has been verified experimentally, and as stated earlier, Cu is the only pure metal that produces $C_{2(+)}$ hydrocarbons, which can be attributed to its moderate adsorption energies for CO* and C*.[16, 34] This observation, is what motivated us to screen the $L1_2$ binary alloys constructed from the mixing of Cu with strong and weak CO binding metals as well as mixing some of the strong CO binding metals $A' \in$ {Fe, Co, Ni, and Pd} with the weaker binding metals *B*. **Figure 2** shows, that the Cu_3A and Cu*A* alloys fall within a similar region as the pure metals *A* with CO* and C* adsorption energies scattered in a related fashion, which is due to the fact that CO* is adsorbed on the top site of the *A* metal and C* is adsorbed at the four-fold site comprised of two Cu atoms and two *A* atoms so that the both the adsorption energies of CO* and C* are strongly dependent on the *A* metals with a small perturbation induced by the Cu environment. For the Cu_3B and Cu*B* alloys the CO* binding energies are less scattered and generally lie very close to that of pure Cu. This is unsurprising, since the favored adsorption site of CO* on Cu_3B (100) and Cu*B* (110) surfaces is an ontop Cu site as shown in the atomic structures at the top and right side of **Figure 2**. The adsorption energy of C* at the four-fold site configured with two Cu and two *B* metal atoms varies more with composition, indicating that the C* adsorption energy can be tuned in a wider range by the introduction of different *B* metals. The B_3A' and BA' alloys are scattered between the Cu_3A (or Cu*A*) and Cu_3B (Cu*B*) regions with more points in the vicinity of Cu. It is noted that for eCO_2R with CO_2(g) as reactant, the $C_{2(+)}$ selectivity map assumes that the material can convert CO_2 into the key intermediate CO* in preference over formate, CO(g), or H_2(g). The CO and OH binding energies can be used to screen for this selectivity as described in Tang *et al*.[47]. The prerequisite of forming CO* is lifted if instead of CO_2, CO is used as reactant in eCOR. Solvation effects via hydrogen bonding with nearby water was considered. For simplicity, we apply a constant solvation correction to all the intermediate species (CO*, COH, C, CH, CCO*, and CHCO*, shown in **Figure 1**) of 0.11 eV based on previous work.[34] It is possible that we underestimate the COH* solvation effects; however, the solvation effect of CO* and C* is negligible;[34] we expect little to no change to the selectivity map in **Figure 2**.

There are several electrochemical models to describe the potential-dependence of an electrochemical reaction.[50-54] Using the computational hydrogen electrode model, which explicitly introduces an energetic correction to electrons on the reversible hydrogen electrode (RHE) scale,[52-54] we can create constant-potential selectivity maps based on the free energies of

G_{C^*} and G_{CO^*} across different metallic alloys. **Figure 3** shows the selectivity map of $L1_2$ and $L1_0$ alloys at different applied potentials, ranging from -1.0 to -0.3 V *vs.* RHE (pH 7). Upon inspection of the Cu_3A alloys, we note that Cu_3Pd has very similar CO* and C* binding energies to those of Cu, thus Cu_3Pd is very likely a good $eCO_{(2)}R$ catalyst for $C_{2(+)}$ product selectivity. In addition, Cu_3Pt and Cu_3Fe are potentially $C_{2(+)}$ selective catalysts at less negative potentials. Most of the Cu_3B alloys have similar CO* binding energies to that of Cu but with weaker C* binding energies (except Cu_3Al and Cu_3Si) and hence they will be unable to produce the intermediate atomic carbon needed in the C-CO coupling mechanism. Among all the Cu_3B alloys, Cu_3Ge and Cu_3Ga are the two alloys that are most similar to Cu, but still with a slightly weaker (0.1 ~ 0.2 eV) CO* adsorption energy which may lead to a much lower rate of CO protonation to COH. In addition, Cu_3Zn, Cu_3Ag, and Cu_3Au that have a more endergonic C* binding energy than Cu could still be $C_{2(+)}$ selective but at more negative applied potentials (< -0.8 V *vs.* RHE at pH 7). It is noted that Cu_3Pb, Cu_3In, and Cu_3Sn have appropriate C* binding energy but a (slightly) weaker CO* binding energy, hence, the Cu-based alloys with *p*-block metals may be good catalysts but share a common issue regarding the weak CO* binding on Cu top sites. We also screened some non-Cu based alloys with good properties for $C_{2(+)}$ selectivity. Ga_3Co, Zn_3Ni, and Al_3Ni indicate some selectivity at less negative applied potential (> -0.6 *vs.* RHE at pH 7); however, these alloys are very close to the thermodynamic boundaries of C-CO coupling and C-H protonation suggesting higher selectivity towards C_1 rather than $C_{2(+)}$ products. Interestingly, a few non-Cu based alloys, like Ga_3Ni, Ga_3Fe, Sn_3Pd, and Ge_3Pd fall into the triangular regions of $C_{2(+)}$ selectivity, implying that they could be promising candidates for $C_{2(+)}$ selective catalysts in $eCO_{(2)}R$. Some other non-Cu based $L1_2$ alloys such as Au_3Pd, Pb_3Pd, and Zn_3Pd should also show enhanced selectivity towards $C_{2(+)}$ products but at slightly lower applied potentials. For the Cu-based $L1_0$ alloys, the Cu*A* alloy of CuPd, and Cu*B* alloys of CuGe and CuZn potentially have good $C_{2(+)}$ selectivity. It is interesting that CuAg and CuAu become less selective towards $C_{2(+)}$ formation than the corresponding Cu-rich $L1_2$ alloys, i.e., Cu_3Ag and Cu_3Au, respectively, because of the weakened C* binding energy at the four-fold site. More non-Cu based alloys are identified as promising candidates; Fe-based alloys like FeZn, FeGa, and FePb, Co-based alloys like CoSn, CoAs, CoSb, and CoSi, Ni-based alloys like NiAs, NiAl, NiIn, NiGa, NiBi, and NiGe, and Pd-based alloys like PdAu and PdAs. We conclude, that the *p*-block elements are important for the Fe, Co, and Ni-based $L1_0$ binary alloys in order to fine tune the key descriptors for the

electroreduction of $CO_{(2)}$ towards $C_{2(+)}$ products. It is worth mentioning that NiAs is found to be a good catalyst, while As_3Ni is outside the $C_{2(+)}$ selective region because of the instability of the As_3Ni surface. In the following, we shall address the stability of the binary alloys.

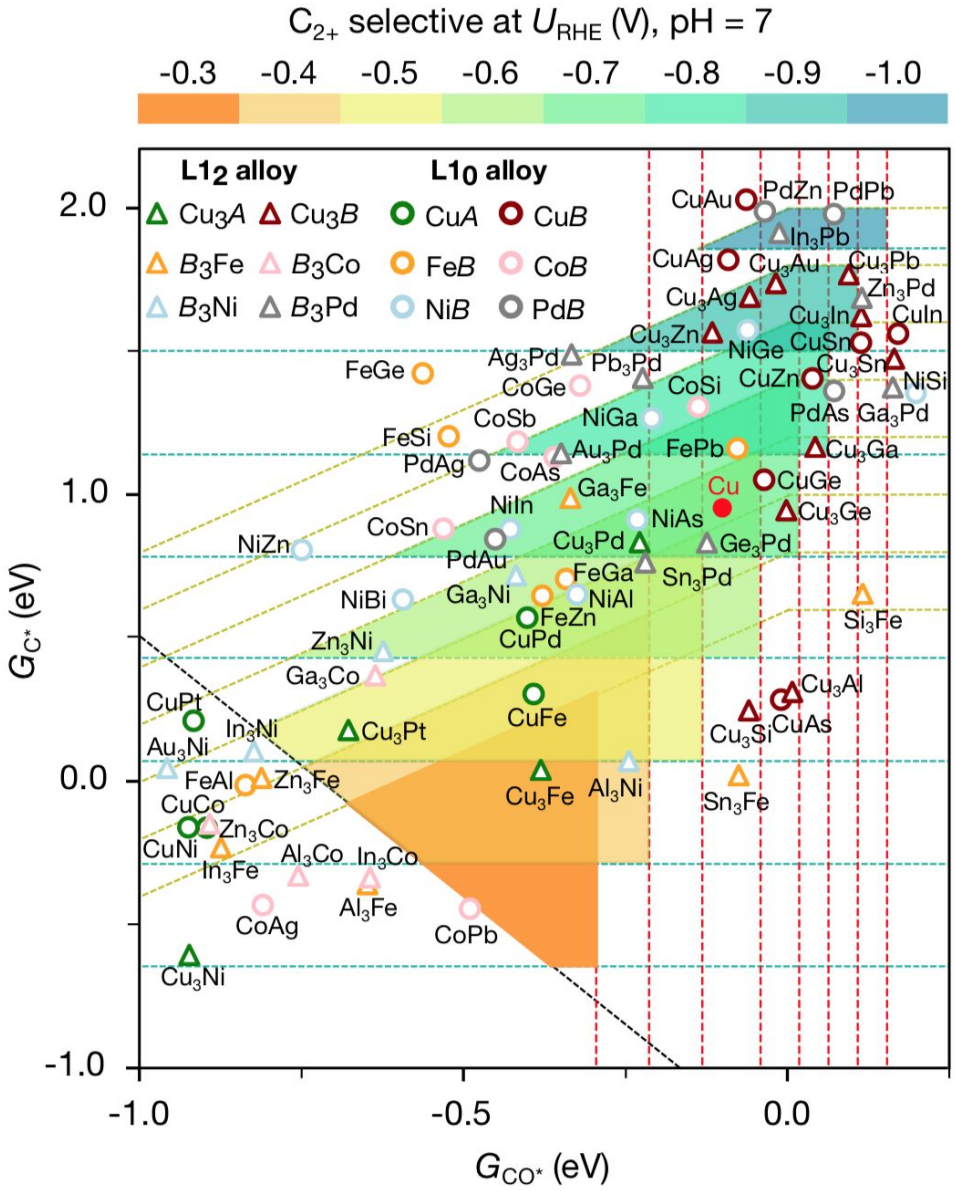

Figure 3 Selectivity map of $L1_2(100)$ and $L1_0(110)$ surfaces at different applied potentials and at pH 7. The triangle markers denote the $L1_2$ binary alloys of Cu_3A (green), Cu_3B (dark red), B_3Fe (orange), B_3Co (pink), B_3Ni (light blue), and B_3Pd (gray). The circle ones are the $L1_0$ alloys of Cu*A* (green), Cu*B*(dark red), *B*Fe (orange), *B*Co (pink), *B*Ni (light blue), and BPd (gray). The selectivity map of $L1_2$ and $L1_0$ alloys at separate potentials are provided in **SI** (see **Figures S1-S4**).

3.2 Surface Formation Energy of Binary Alloy

It is widely accepted that synthesizing alloys with a specific metal ratio is pretty challenging with existing methods such as liquid-phase syntheses, metallic fusion, and electrochemical deposition, especially when two metals have different surface energies.[24, 55-58] Surface phase diagram and surface segregation energy are widely used to investigate the stability of alloy surfaces.[59-60] However, for simplification, in this work, the surface formation energy (E_{sfe}) is used to evaluate the stability of the binary alloy surfaces, which is defined to be the formational energy gain (or loss) of the alloyed surface relative to the pure surfaces of the dopant metal and the host metal, i.e.,

$$E_{\mathrm{sfe}} = E_{\mathrm{DFT}}\left(M_x M'_y\right)/N_0 - \left(\frac{x}{x+y}\right) \cdot E_{\mathrm{DFT}}(M)/N_1 - \left(\frac{y}{x+y}\right) \cdot E_{\mathrm{DFT}}(M')/N_2$$

where $E_{\mathrm{DFT}}\left(M_x M'_y\right)$ is the DFT energy of the binary alloy slab ($M_x M'_y$) with a total number of N_0 atoms ($N_0 = x + y$). x and y are, respectively, the number of M and M' metal atoms in the binary alloy slab. $E_{\mathrm{DFT}}(M)$ and $E_{\mathrm{DFT}}(M')$ are the DFT energies of pure M and M' slabs, respectively, with N_1 and N_2 atoms in the corresponding pure metal slabs,.

Based on the above definition, we calculate the formation energies for the clean $L1_2$ and $L1_0$ alloy surfaces. The results are shown in **Figure 4**.

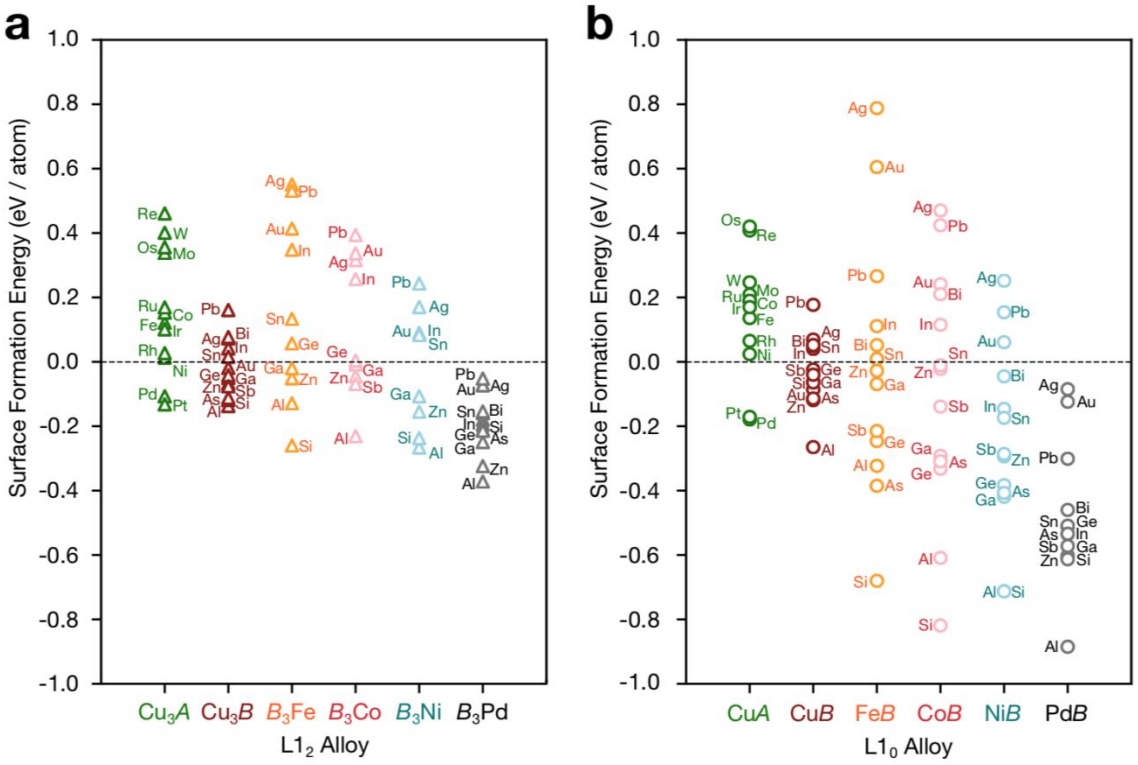

Figure 4 Formation energies of (a) $L1_2$ (100) and (b) $L1_0$ (110) clean surfaces. Some of the binary alloys, mainly the Fe, Co, and Ni-based alloys, are not shown in the figure because of the severe reconstruction or decomposition during the DFT geometry optimization. These omitted alloys are considered unstable. The same stability data shown in this figure is also plotted in bar plots (see **Figures S5** and **S6**).

Most of the Cu-based Cu_3A binary $L1_2$ alloys are unstable with exceptions of Cu_3Pd and Cu_3Pt. We note that the formation energies mentioned here are evaluated entirely on the clean surfaces. If the surfaces are covered with CO, the interaction of CO with *A* and Cu atoms may decrease the stability of the Cu_3A alloy surfaces.[61] The stabilities of the Cu-based Cu_3B alloys are overall better than those of the Cu_3A alloys, and only the Cu_3Ag, Cu_3In, Cu_3Pb, and Cu_3Bi are unstable. The Fe, Co, and Ni-based alloys show a similar trend that the alloys with the *B* metals Ag, Au, In, Ge, Sn, and Pb are very unstable. In comparison, the Ni-based alloys are more stable than the Co-based alloys followed by the Fe-based alloys. It is encouraging that all the Pd-based alloys are stable as many of these show promising selectivity properties. The overall trends of the stabilities of the $L1_0$ alloys are very similar to those of the $L1_2$ alloys, especially for the Cu-based $Cu_{(3)}A$ and $Cu_{(3)}B$ alloys, as shown in **Figure 4**; however, for the Fe, Co, Ni, and Pd-based alloys, the $L1_0$ alloys are more stable than the $L1_2$ alloys. Therefore, reducing the ratio of the weakly CO binding *B* metal to the *A′* metal enhances the stability of the non-Cu based alloys.

3.3 Comparison of Experimental Observations with Theoretic Findings

Despite the challenges of forming alloys with specific metal ratios, there are a number of experimental studies available for binary alloys applied in eCO_2R. In the following, we shall compare these experimental observations with our theoretical findings.

3.3.1 Cu-based Alloys

- **Cu-Au alloy**

Kim *et al.*[62] investigated the Cu-Au alloys with different ratios of Cu to Au and quantitatively compared the selectivity and activity as a function of Au content. No C_2 products are found for the pure Au and $CuAu_3$. C_2 products of ethanol and ethylene are produced with the CuAu and Cu_3Au alloys with onset potential of ~ -0.9 V *vs.* RHE. In comparison, the Cu_3Au performs better than the CuAu in terms of C_2 selectivity. Our theoretical screening result illustrates this tendency, as shown in **Figures 3**; with increasing Au content, the binding energy of C* becomes less stable, making it difficult to form C* from CO* through protonation. Wang *et al.*[63] synthesized an Au-poor Cu-Au alloy (7% Au atomic percentage) and obtained a Faradaic efficiency (FE) of ethylene as high as 40% at -1.15 V *vs.* RHE and a further decrease of the potential to -1.25 V *vs.* RHE leads to methane as the major product instead of ethylene, in line with the theoretical results herein.

- **Cu-Ag alloy**

Lee *et al.*[64] investigated the Cu-Ag alloys for eCO_2R with ratios of Cu to Ag close to 3:1. The phase-blended Cu-Ag alloy shows a three times higher FE of ethanol than that of pure Cu. The onset potential of the C_2 products (ethanol and ethylene) is about -0.9 V and reaches the highest FE of ethanol (up to 30%) at -1.2 V *vs.* RHE. This experimental observation is consistent with our theoretical finding that the Cu_3Ag alloy should be a good $CO_{(2)}$ electrocatalyst for $C_{2(+)}$ products at more negative potentials (< -0.8 V *vs.* RHE). In addition, it is observed by Lee *et al.*[64] and others[22, 61] that there is a surface segregation in the Cu-Ag alloy, which can be explained through our theoretical findings that the formation energy of the Cu_3Ag (100) surface is slightly positive (0.07 eV/atom) referenced to the pure Cu(100) and Ag(100) surface energies.

- **Cu-Zn alloy**

Ren *et al.*[65] studied Cu-Zn alloys with different amounts of Zn ($Cu_{10}Zn$, Cu_4Zn, and Cu_2Zn) and found that the Cu_4Zn shows the maximum ethanol formation at -1.05 V *vs.* RHE with pretty high FE of 29.1% and current density of -8.2 mA/cm^2. Our theoretical screening shows that both

Cu_3Zn and CuZn are potentially good $C_{2(+)}$ selective catalysts under very negative potentials and comparatively, Cu_3Zn has a very similar CO* binding energy to that of pure Cu whereas CuZn shows a 0.14 eV weaker binding of CO*.

- **Cu-Pd alloy**

Ma *et al.*[66] systematically studied the Cu-Pd alloys with different atomic ratios and different mixing patterns (ordered, disordered, and phase-separated). The phase-separated Cu-Pd shows the highest FE (up to 63%) of C_2 products with an onset potential as low as -0.3 V *vs.* RHE. For the disordered Cu-Pd alloys, Cu_3Pd perform better than CuPd in C_2 selectivity. Our theoretical findings reveal that both Cu_3Pd and CuPd are C_2 selective at a more positive onset potential than that of Cu. Furthermore, Cu_3Pd is more Cu-like than CuPd, which agrees well with the above-mentioned observations.

- **Cu-Sn alloy**

Sarfraz *et al.*[67] reported the Cu-Sn alloy for selective reduction of CO_2 to CO with high Faradaic efficiency (FE) (> 90%) and found that Sn in the surface layer suppresses the HER competing with eCO_2R. The increased CO selectivity can be explained with our theoretical finding that Cu_3Sn has an appropriate C* binding energy but a weaker CO* adsorption energy than that on Cu so that Cu_3Sn is outside the $C_{2(+)}$ selective region but performs well for CO_2 reduction to CO.

- **Cu-In alloy**

Larrazábal *et al.*[68] investigated the Cu-In alloy as electrocatalyst for CO_2R and found that the structurally evolved Cu-In core-shell nanoparticles catalyzes eCO_2R with CO as the major product. This observation can be understood from two aspects of our theoretical findings. Firstly, the Cu_3In and CuIn alloys both have weak CO* binding energies, as shown in **Figure 3**. Secondly, both the Cu_3In and CuIn are unstable with formation energies of about 0.04 eV/atom (**Figure 4**), thus indicating that the Cu-In alloy could evolve into a core-shell nanoparticle structure with In-species aggregated on the surface.

Furthermore, Larrazábal *et al.*[69] reported the Cu-based alloys with introduction of p-black elements (Sn, In, Ga, Al) in a small amount (< 8 wt. %) and found the Cu-Al (0.3 wt.%) shows some C_2 selectivity. Besides the above-mentioned Cu-based alloys reported in recent years, some other Cu-based alloys (e.g., Cu-Ni, Cu-Pb, Cu-Cd) were reported by Watanabe and coworkers in the early 90s.[70]

3.3.2 Non-Cu Based Alloys

Compared with the Cu-based alloys, only a few non-Cu based alloys have been reported in the context of eCO_2R.

- **Ni-Ga alloy**

Torelli *et al.*[71] reported three different Ni-Ga alloys (NiGa, Ni_3Ga, and Ni_5Ga_3) active in eCO_2R and found that all these three alloys have the similar C_2 onset potentials (-0.48 V *vs.* RHE) and product distributions. The FEs of C_2 products reach the peaks of ~1.7% and ~0.4% at -0.88 V (*vs.* RHE) for C_2H_6 and C_2H_4, respectively. Our theoretical findings show that both Ga_3Ni and NiGa are C_2 selective (**Figure 3**) and stable (**Figure 4a and 4b**); however, based on our results, Ga_3Ni is predicted to have a more positive onset potential than Cu while NiGa is predicted to have a more negative onset potential.

- **Pd-Sn alloy**

Bai *et al.*[72] tested a series of Pd-Sn alloys. It shows that the content of Sn in the Pd-Sn alloys has a significant effect on the product distribution. The 1:1 Pd-Sn alloy exhibits a higher than 95% FE toward formic acid production at a very low overpotential of -0.26 V. Our theoretical study reveals that the PdSn alloy has high binding energies for both CO* and C* (see **SI**, **Table S2**); suggesting that it is difficult to drive formation of any $C_{2(+)}$ products. Calculation of the OH* stability and its ability to induce segregation could shed further light on the enhanced selectivity towards formic acid.[47]

- **Pd-Au alloy**

Valenti *et al.*[73] studied several Pd-Au alloys including Au_3Pd and AuPd for eCO_2R and reported production of CO and some H_2 on these systems. This observation is inconsistent with our theoretical findings, where both Au_3Pd and AuPd are close to (or in) the C_2 selective triangles (**Figure 3**). This could be due to the enhanced instability of Pd-Au alloys compared with other Pd-based alloys (**Figure 4**) but clearly needs further investigation.

3.3.3 Summary of the Screened-out Alloys

Combing the information from the selectivity map in **Figures 3** with the stability shown in **Figure 4**, we summarize the $C_{2(+)}$ selectivity and stability of the $L1_2$ and $L1_0$ alloys in **Table 1**.

Table 1 $C_{2(+)}$ selective $L1_2$ and $L1_0$ alloys at different applied potential ranges U (V *vs.* RHE at pH 7). The alloys in parenthesis are unstable and the ones in bold font have been reported experimentally for $eCO_{(2)}R$.

Structure	Type	-1.1 V< U < -0.8 V	-0.8 V < U < -0.6 V	-0.6 V < U < -0.3 V
$L1_2$ alloys	Cu_3A		**Cu_3Pd**	Cu_3Pt, (Cu_3Fe)
	Cu_3B	**Cu_3Zn**, **Cu_3Au**, (**Cu_3Ag**, **Cu_3In**, Cu_3Pb)	Cu_3Ge, Cu_3Ga	
	B_3Fe		Ga_3Fe	
	B_3Co			Ga_3Co
	B_3Ni		**Ga_3Ni**, Zn_3Ni	Al_3Ni
	B_3Pd	Pb_3Pd, Zn_3Pd, In_3Pd	Ge_3Pd, **Au_3Pd**	Sn_3Pd
$L1_0$ alloys	CuA		**CuPd**	(CuFe)
	CuB	(**CuSn**), (**CuAg**)	CuGe, **CuZn**	
	FeB		FeGa, FeZn, (FePb)	
	CoB		CoSi, CoSn, CoAs, CoSb, CoGe	
	NiB	NiGe	NiAs, **NiGa**, NiIn, NiAl NiBi	
	PdB	PdAs, PdZn, PdPb	**PdAu**	

In **Table 1**, few a (shown in bold fonts) of the screened-out binary alloys have been experimentally reported, which are mainly Cu-based alloys. Most of our screened-out non-Cu based alloys are of great interest to be tested. Based on our theoretical findings, the *p*-block elements (e.g., Ga, Ge, As, Si, Al) play a significant role in constituting the non-Cu based $C_{2(+)}$ selective binary alloys.

It's noted that we only investigated the ideal adsorption sites on $L1_2(100)$ and $L1_0(110)$ surfaces, whereas a real alloy catalyst surface is more complicated with distributions of sites as investigated by Gauthier *et al*.[74]. Nevertheless, our theoretical screening not only successfully reidentifies the alloys known to have good C_{2+} selectivity, but also discovers several materials with promising properties that have not previously been tested in $eCO_{(2)}R$.

4. Conclusions

A $C_{2(+)}$ selectivity map generated based on thermodynamic conditions of key steps in the reaction network is a powerful tool when screening for possible catalyst compositions. In this work, a number of $L1_2$ and $L1_0$ binary alloys comprised of strongly or weakly CO binding metals

have been explored as electrocatalysts for $eCO_{(2)}R$ towards $C_{2(+)}$ species. We have found that the Cu-*A* (Cu_3A and Cu*A*) alloys fall within a similar region as pure *A* metals, where *A* belongs to the strong CO* binding group of metals, and that the adsorption energies of CO* and C* are strongly dependent on the *A* metal in the composition and the perturbing effect of the Cu environment. Comparatively, the Cu-*B* (Cu_3B and Cu*B*) alloys, where *B* belongs to the weak CO* binding group of metals, distribute less scattered, especially the CO* binding energies are very close to that of pure Cu, and the C* adsorption energy can be tuned to some degree by incorporating different *B* metals. For the $C_{2(+)}$ selective Cu-based alloys, we have identified the (100)-terminated $L1_2$ alloys of Cu_3Pd, Cu_3Pt, Cu_3Fe, Cu_3Zn, Cu_3Ag, Cu_3Au, Cu_3Ge, Cu_3Ga, Cu_3In, and Cu_3Pb, and the (110)-terminated $L1_0$ alloys of CuPd, CuFe, CuAg, CuZn, CuGe, and CuSn. These alloys have different onset potentials for $C_{2(+)}$ production. Generally, the Cu-*A* alloys, e.g., Cu_3Pt, Cu_3Fe, and CuFe, have more positive onset potentials than pure Cu, while the Cu-*B* alloys have more negative onset potentials. We also identified about 11 non-Cu based $L1_2$ alloys and 18 non-Cu based $L1_0$ alloys, e.g., Ga_3Ni, Ga_3Fe, Ge_3Pd, NiAs, NiAl, CoSi, most of which are comprised of Fe, Co, Ni, and Pd alloyed with *p*-block elements. Therefore, we conclude that the use of *p*-block elements in Fe, Co, and Ni-based binary alloys is promising for fine-tuning the key descriptors (C* and CO*) for $eCO_{(2)}R$ towards $C_{2(+)}$ products. In addition, we studied the stability of the binary alloys by analyzing the formation energy of the clean alloy surfaces. Most of the Cu-*A* binary alloys are unstable with the exception of $Cu_{(3)}Pd$ and $Cu_{(3)}Pt$. The stability of the Cu-*B* alloys is overall better than for the Cu-*A* alloys, and only the $Cu_{(3)}Ag$, $Cu_{(3)}In$, $Cu_{(3)}Sn$, $Cu_{(3)}Pb$, and $Cu_{(3)}Bi$ are found to be unstable. The Fe, Co, and Ni-based $L1_0$ alloys show a similar trend, as the alloys with Ag, Au, In, Ge, Sn, and Pb are found to be unstable. We find that all the Pd-based alloys are stable. Of the stable Fe, Co, Ni, and Pd-based structures, the $L1_0$ alloys are observed to be more stable than the corresponding $L1_2$ alloys, in other words reducing the ratio of the weakly CO binding *B* metal to the Fe, Co, Ni, or Pd metal enhances the stability of the non-Cu based alloys. The stability and $C_{2(+)}$ selectivity of some of our screened binary alloys have been validated experientially and in majority of the cases, our theoretical findings are in line with the experimental observations. In particular, we encourage experimental investigations of the highlighted (non-bolded) materials in **Table 1**. These have, to the best of our knowledge, not been evaluated in $eCO_{(2)}R$ but show promising properties both in terms of stability and for selectivity towards the much sought after C_{2+} products.

5. Acknowledgements

This material is based on work performed by the Liquid Sunlight Alliance, which is supported by the US Department of Energy, Office of Science, Office of Basic Energy Sciences, and Fuels from Sunlight Hub under award no. DE-SC0021266. JHS acknowledge support from the Knut and Alice Wallenberg Foundation (grant nr. 2019.0586). The authors would also like to acknowledge the use of the computer time allocation for the material simulations in the Liquid Sunlight Alliance (LiSA) at the National Energy Research Scientific Computing Center, a DOE Office of Science User Facility supported by the Office of Science of the U.S. Department of Energy under Contract No. DE-AC02-05CH11231.

6. Conflicts of interest

There are no conflicts of interest to declare.

References

(1) Vasileff, A.; Xu, C.; Jiao, Y.; Zheng, Y.; Qiao, S. Z. Surface and interface engineering in copper-based bimetallic materials for selective CO_2 electroreduction. *Chem* **2018,** *4*, 1809-1831.
(2) Raciti, D.; Wang, C. Recent advances in CO_2 reduction electrocatalysis on copper. *ACS Energy Lett.* **2018,** *3*, 1545-1556.
(3) Ozin, G. A. Throwing new light on the reduction of CO_2. *Adv. Mater.* **2015,** *27*, 1957-1963.
(4) Agarwal, A. S.; Zhai, Y.; Hill, D.; Sridhar, N. The electrochemical reduction of carbon dioxide to formate/formic acid: engineering and economic feasibility. *ChemSusChem* **2011,** *4*, 1301-1310.
(5) Zhang, S.; Fan, Q.; Xia, R.; Meyer, T. J. CO_2 reduction: from homogeneous to heterogeneous electrocatalysis. *Acc. Chem. Res.* **2020,** *53*, 255-264.
(6) Jalid, F.; Khan, T. S.; Haider, M. A. Exploring bimetallic alloy catalysts of Co, Pd and Cu for CO_2 reduction combined with ethane dehydrogenation. *Appl. Energy* **2021,** *299*, 117284.
(7) Tsiotsias, A. I.; Charisiou, N. D.; Yentekakis, I. V.; Goula, M. A. Bimetallic Ni-Based Catalysts for CO_2 Methanation: A Review. *Nanomaterials* **2021,** *11*, 28.
(8) Chu, S.; Cui, Y.; Liu, N. The path towards sustainable energy. *Nat. Mater.* **2017,** *16*, 16-22.
(9) Lee, C. W.; Yang, K. D.; Nam, D. H.; Jang, J. H.; Cho, N. H.; Im, S. W.; Nam, K. T. Defining a materials database for the design of copper binary alloy catalysts for electrochemical CO_2 conversion. *Adv. Mater.* **2018,** *30*, 1704717.
(10) Senftle, T. P.; Carter, E. A. The holy grail: chemistry enabling an economically viable CO_2 capture, utilization, and storage strategy. *Acc. Chem. Res.* **2017,** *50*, 472-475.
(11) Hu, Y.; Chen, F.; Ding, P.; Yang, H.; Chen, J.; Zha, C.; Li, Y. Designing effective Si/Ag interface via controlled chemical etching for photoelectrochemical CO_2 reduction. *J. Mater. Chem. A* **2018,** *6*, 21906-21912.

(12) Kauffman, D. R.; Thakkar, J.; Siva, R.; Matranga, C.; Ohodnicki, P. R.; Zeng, C.; Jin, R. Efficient electrochemical CO_2 conversion powered by renewable energy. *ACS Appl. Mater. Interfaces* **2015,** *7*, 15626-15632.
(13) Qiao, J.; Liu, Y.; Hong, F.; Zhang, J. A review of catalysts for the electroreduction of carbon dioxide to produce low-carbon fuels. *Chem. Soc. Rev* **2014,** *43*, 631-675.
(14) Kim, D.; Kley, C. S.; Li, Y.; Yang, P. Copper nanoparticle ensembles for selective electroreduction of CO_2 to C_2-C_3 products. *Proc. Natl. Acad. Sci. U.S.A.* **2017,** *114*, 10560-10565.
(15) De Luna, P.; Hahn, C.; Higgins, D.; Jaffer, S. A.; Jaramillo, T. F.; Sargent, E. H. What would it take for renewably powered electrosynthesis to displace petrochemical processes? *Science* **2019,** *364*.
(16) Nitopi, S.; Bertheussen, E.; Scott, S. B.; Liu, X.; Engstfeld, A. K.; Horch, S.; Seger, B.; Stephens, I. E.; Chan, K.; Hahn, C.; Nørskov, J. K. Progress and perspectives of electrochemical CO_2 reduction on copper in aqueous electrolyte. *Chem. Rev.* **2019,** *119*, 7610-7672.
(17) Whipple, D. T.; Kenis, P. J. Prospects of CO_2 utilization via direct heterogeneous electrochemical reduction. *J. Phys. Chem. Lett.* **2010,** *1*, 3451-3458.
(18) Martín, A. J.; Larrazábal, G. O.; Pérez-Ramírez, J. Towards sustainable fuels and chemicals through the electrochemical reduction of CO_2: lessons from water electrolysis. *Green Chem.* **2015,** *17*, 5114-5130.
(19) Costentin, C.; Robert, M.; Savéant, J. M. Catalysis of the electrochemical reduction of carbon dioxide. *Chem. Soc. Rev.* **2013,** *42*, 2423-2436.
(20) Peterson, A. A.; Nørskov, J. K. Activity descriptors for CO_2 electroreduction to methane on transition-metal catalysts. *J. Phys. Chem. Lett.* **2012,** *3*, 251-258.
(21) Kuhl, K. P.; Hatsukade, T.; Cave, E. R.; Abram, D. N.; Kibsgaard, J.; Jaramillo, T. F. Electrocatalytic conversion of carbon dioxide to methane and methanol on transition metal surfaces. *J. Am. Chem. Soc.* **2014,** *136*, 14107-14113.
(22) Chang, Z.; Huo, S.; Zhang, W.; Fang, J.; Wang, H. The tunable and highly selective reduction products on Ag@Cu bimetallic catalysts toward CO_2 electrochemical reduction reaction. *J. Phys. Chem. C* **2017,** *121*, 11368-11379.
(23) Grote, J. P.; Zeradjanin, A. R.; Cherevko, S.; Savan, A.; Breitbach, B.; Ludwig, A.; Mayrhofer, K. J. Screening of material libraries for electrochemical CO_2 reduction catalysts–Improving selectivity of Cu by mixing with Co. *J. Catal.* **2016,** *343*, 248-256.
(24) He, J.; Dettelbach, K. E.; Salvatore, D. A.; Li, T.; Berlinguette, C. P. High-throughput synthesis of mixed-metal electrocatalysts for CO_2 reduction. *Angew. Chem. Int. Ed.* **2017,** *129*, 6164-6168.
(25) Hammer, B.; Nørskov, J. K. Electronic factors determining the reactivity of metal surfaces. *Surf. Sci.* **1995,** *343*, 211-220.
(26) Hammer, B.; Norskov, J. K. Why gold is the noblest of all the metals. *Nature* **1995,** *376*, 238-240.
(27) Xin, H.; Vojvodic, A.; Voss, J.; Nørskov, J. K.; Abild-Pedersen, F. Effects of d-band shape on the surface reactivity of transition-metal alloys. *Phys. Rev. B* **2014,** *89*, 115114.
(28) Bagger, A.; Ju, W.; Varela, A. S.; Strasser, P.; Rossmeisl, J. Electrochemical CO_2 reduction: a classification problem. *ChemPhysChem* **2017,** *18*, 3266-3273.
(29) Bagger, A.; Ju, W.; Varela, A. S.; Strasser, P.; Rossmeisl, J. Electrochemical CO_2 reduction: classifying Cu facets. *ACS Catal.* **2019,** *9*, 7894-7899.
(30) Zhi, X.; Jiao, Y.; Zheng, Y.; Vasileff, A.; Qiao, S. Z. Selectivity roadmap for electrochemical CO_2 reduction on copper-based alloy catalysts. *Nano Energy* **2020,** *71*, 104601.

(31) Zhao, Z.; Chen, Z.; Lu, G. Computational discovery of nickel-based catalysts for CO_2 reduction to formic acid. *J. Phys. Chem. C* **2017,** *121*, 20865-20870.
(32) Ma, X.; Li, Z.; Achenie, L. E.; Xin, H. Machine-learning-augmented chemisorption model for CO_2 electroreduction catalyst screening. *J. Phys. Chem. Lett.* **2015,** *6*, 3528-3533.
(33) Tran, K.; Ulissi, Z. W. Active learning across intermetallics to guide discovery of electrocatalysts for CO_2 reduction and H_2 evolution. *Nat. Catal.* **2018,** *1*, 696-703.
(34) Peng, H.; Tang, M. T.; Liu, X.; Lamoureux, P. S.; Bajdich, M.; Abild-Pedersen, F. The role of atomic carbon in directing electrochemical $CO_{(2)}$ reduction to multicarbon products. *Energy Environ. Sci.* **2021,** *14*, 473-482.
(35) Leroux, C.; Loiseau, A.; Broddin, D.; Vantendeloo, G. Electron microscopy study of the coherent two-phase mixtures $L1_0 + L1_2$, in Co-Pt alloys. *Philos. Mag. B* **1991,** *64*, 57-82.
(36) Pankratov, I.; Vaks, V. G. Kinetics of $L1_0$-type and $L1_2$-type orderings in alloys at early stages of phase transformations. *J. Phys.: Condens. Matter* **2001,** *13*, 6031.
(37) Ozoliņš, V.; Wolverton, C.; Zunger, A. First-principles theory of vibrational effects on the phase stability of Cu-Au compounds and alloys. *Phys. Rev. B* **1998,** *58*, R5897.
(38) Giannozzi, P.; Baroni, S.; Bonini, N.; Calandra, M.; Car, R.; Cavazzoni, C.; Ceresoli, D.; Chiarotti, G. L.; Cococcioni, M.; Dabo, I.; Dal Corso, A.; de Gironcoli, S.; Fabris, S.; Fratesi, G.; Gebauer, R.; Gerstmann, U.; Gougoussis, C.; Kokalj, A.; Lazzeri, M.; Martin-Samos, L.; Marzari, N.; Mauri, F.; Mazzarello, R.; Paolini, S.; Pasquarello, A.; Paulatto, L.; Sbraccia, C.; Scandolo, S.; Sclauzero, G.; Seitsonen, A. P.; Smogunov, A.; Umari, P.; Wentzcovitch, R. M. QUANTUM ESPRESSO: a modular and open-source software project for quantum simulations of materials. *J. Phys.: Condens. Matter* **2009,** *21*, 395502.
(39) Bahn, S. R.; Jacobsen, K. W. An object-oriented scripting interface to a legacy electronic structure code. *Comput. Sci. Eng.* **2002,** *4*, 56-66.
(40) Wellendorff, J.; Lundgaard, K. T.; Mogelhoj, A.; Petzold, V.; Landis, D. D.; Nørskov, J. K.; Bligaard, T.; Jacobsen, K. W. Density functionals for surface science: Exchange-correlation model development with Bayesian error estimation. *Phys. Rev. B* **2012,** *85*, 235149.
(41) Monkhorst, H. J.; Pack, J. D. Special points for Brillouin-zone integrations. *Phys. Rev. B* **1976,** *13*, 5188-5192.
(42) Vanderbilt, D. Soft self-consistent pseudopotentials in a generalized eigenvalue formalism. *Phys. Rev. B* **1990,** *41*, 7892.
(43) Bengtsson, L. Dipole correction for surface supercell calculations. *Phys. Rev. B* **1999,** *59*, 12301.
(44) Gajdoš, M.; Eichler, A.; Hafner, J. CO adsorption on close-packed transition and noble metal surfaces: trends from ab initio calculations. *J. Phys.: Condens. Matter* **2004,** *16*, 1141-1164.
(45) Abild-Pedersen, F.; Andersson, M. P. CO adsorption energies on metals with correction for high coordination adsorption sites - A density functional study. *Surf. Sci.* **2007,** *601*, 1747-1753.
(46) Winther, K. T.; Hoffmann, M. J.; Boes, J. R.; Mamun, O.; Bajdich, M.; Bligaard, T. Catalysis-Hub.org an open electronic structure database for surface reactions. *Sci. Data* **2019,** *6*, 75.
(47) Tang, M. T.; Peng, H.; Lamoureux, P. S.; Bajdich, M.; Abild-Pedersen, F. From electricity to fuels: Descriptors for C_1 selectivity in electrochemical CO_2 reduction. *Appl. Catal. B* **2020,** *279*, 119384.

(48) Zijlstra, B.; Zhang, X.; Liu, J. X.; Filot, I. A.; Zhou, Z.; Sun, S.; Hensen, E. J. First-principles microkinetics simulations of electrochemical reduction of CO_2 over Cu catalysts. *Electrochim. Acta* **2020,** *335*, 135665.
(49) Li, S.; Sun, S.; Suo, W.; Liu, G.; Wang, G.; Wang, Y.; Li, J.; Zhang, Z. Theoretical investigation of electrochemical reduction mechanism of CO_2 on the Cu(111), Sn@Cu(111) and Sn(211) surfaces. *Appl. Surf. Sci.* **2021,** *564*, 150418.
(50) Goodpaster, J. D.; Bell, A. T.; Head-Gordon, M. Identification of possible pathways for C–C bond formation during electrochemical reduction of CO2: new theoretical insights from an improved electrochemical model. *J. Phys. Chem. Lett.* **2016,** *7*, 1471-1477.
(51) Gauthier, J. A.; Ringe, S.; Dickens, C. F.; Garza, A. J.; Bell, A. T.; Head-Gordon, M.; Nørskov, J. K.; Chan, K. Challenges in modeling electrochemical reaction energetics with polarizable continuum models. *ACS Catal.* **2018,** *9*, 920-931.
(52) Skúlason, E.; Tripkovic, V.; Björketun, M. E.; Gudmundsdottir, S.; Karlberg, G.; Rossmeisl, J.; Bligaard, T.; Jónsson, H.; Nørskov, J. K. Modeling the electrochemical hydrogen oxidation and evolution reactions on the basis of density functional theory calculations. *J. Phys. Chem. C* **2010,** *114*, 18182-18197.
(53) Skúlason, E.; Karlberg, G. S.; Rossmeisl, J.; Bligaard, T.; Greeley, J.; Jónsson, H.; Nørskov, J. K. Density functional theory calculations for the hydrogen evolution reaction in an electrochemical double layer on the Pt (111) electrode. *Phys. Chem. Chem. Phys.* **2007,** *9*, 3241-3250.
(54) Skúlason, E. Modeling electrochemical reactions at the solid-liquid interface using density functional calculations. *Procedia Comput. Sci.* **2015,** *51*, 1887-1896.
(55) Smith, R. D.; Prévot, M. S.; Fagan, R. D.; Zhang, Z.; Sedach, P. A.; Siu, M. K. J.; Trudel, S.; Berlinguette, C. P. Photochemical route for accessing amorphous metal oxide materials for water oxidation catalysis. *Science* **2013,** *340*, 60-63.
(56) Smith, R. D.; Prévot, M. S.; Fagan, R. D.; Trudel, S.; Berlinguette, C. P. Water oxidation catalysis: electrocatalytic response to metal stoichiometry in amorphous metal oxide films containing iron, cobalt, and nickel. *J. Am. Chem. Soc.* **2013,** *135*, 11580-11586.
(57) Wang, D.; Li, Y. Bimetallic nanocrystals: liquid-phase synthesis and catalytic applications. *Adv. Mater.* **2011,** *23*, 1044-1060.
(58) Zangari, G. Electrodeposition of alloys and compounds in the era of microelectronics and energy conversion technology. *Coatings* **2015,** *5*, 195-218.
(59) Christensen, A.; Ruban, A.; Stoltze, P.; Jacobsen, K. W.; Skriver, H. L.; Nørskov, J. K.; Besenbacher, F. Phase diagrams for surface alloys. *Phys. Rev. B* **1997,** *56*, 5822-5834.
(60) Ruban, A.; Skriver, H. L.; Nørskov, J. K. Surface segregation energies in transition-metal alloys. *Phys. Rev. B* **1999,** *59*, 15990-16000.
(61) Clark, E. L.; Hahn, C.; Jaramillo, T. F.; Bell, A. T. Electrochemical CO_2 reduction over compressively strained CuAg surface alloys with enhanced multi-carbon oxygenate selectivity. *J. Am. Chem. Soc.* **2017,** *139*, 15848-15857.
(62) Kim, D.; Resasco, J.; Yu, Y.; Asiri, A. M.; Yang, P. Synergistic geometric and electronic effects for electrochemical reduction of carbon dioxide using gold-copper bimetallic nanoparticles. *Nat. Commun.* **2014,** *5*, 1-8.
(63) Wang, X.; Ou, P.; Wicks, J.; Xie, Y.; Wang, Y.; Li, J.; Tam, J.; Ren, D.; Howe, J. Y.; Wang, Z. Gold-in-copper at low *CO coverage enables efficient electromethanation of CO_2. *Nat. Commun.* **2021,** *12*, 1-7.

(64) Lee, S.; Park, G.; Lee, J. Importance of Ag-Cu biphasic boundaries for selective electrochemical reduction of CO_2 to ethanol. *ACS Catal.* **2017,** *7*, 8594-8604.
(65) Ren, D.; Ang, B. S. H.; Yeo, B. S. Tuning the selectivity of carbon dioxide electroreduction toward ethanol on oxide-derived Cu_xZn catalysts. *ACS Catal.* **2016,** *6*, 8239-8247.
(66) Ma, S.; Sadakiyo, M.; Heima, M.; Luo, R.; Haasch, R. T.; Gold, J. I.; Yamauchi, M.; Kenis, P. J. Electroreduction of carbon dioxide to hydrocarbons using bimetallic Cu-Pd catalysts with different mixing patterns. *J. Am. Chem. Soc.* **2017,** *139*, 47-50.
(67) Sarfraz, S.; Garcia-Esparza, A. T.; Jedidi, A.; Cavallo, L.; Takanabe, K. Cu–Sn bimetallic catalyst for selective aqueous electroreduction of CO_2 to CO. *ACS Catal.* **2016,** *6*, 2842-2851.
(68) Larrazábal, G. n. O.; Martín, A. J.; Mitchell, S.; Hauert, R.; Pérez-Ramírez, J. Enhanced reduction of CO_2 to CO over Cu-In electrocatalysts: catalyst evolution is the key. *ACS Catal.* **2016,** *6*, 6265-6274.
(69) Larrazábal, G. O.; Martín, A. J.; Krumeich, F.; Hauert, R.; Pérez-Ramírez, J. Solvothermally-Prepared Cu_2O Electrocatalysts for CO_2 Reduction with Tunable Selectivity by the Introduction of p-Block Elements. *ChemSusChem* **2017,** *10*, 1255-1265.
(70) Watanabe, M.; Shibata, M.; Katoh, A.; Sakata, T.; Azuma, M. Design of alloy electrocatalysts for CO_2 reduction. *J. Electroanal. Chem.* **1991,** *305*, 319-328.
(71) Torelli, D. A.; Francis, S. A.; Crompton, J. C.; Javier, A.; Thompson, J. R.; Brunschwig, B. S.; Soriaga, M. P.; Lewis, N. S. Nickel-gallium-catalyzed electrochemical reduction of CO_2 to highly reduced products at low overpotentials. *ACS Catal.* **2016,** *6*, 2100-2104.
(72) Bai, X.; Chen, W.; Zhao, C.; Li, S.; Song, Y.; Ge, R.; Wei, W.; Sun, Y. Exclusive formation of formic acid from CO_2 electroreduction by a tunable Pd-Sn alloy. *Angew. Chem. Int. Ed.* **2017,** *129*, 12387-12391.
(73) Valenti, M.; Prasad, N. P.; Kas, R.; Bohra, D.; Ma, M.; Balasubramanian, V.; Chu, L.; Gimenez, S.; Bisquert, J.; Dam, B.; Smith, W.A. Suppressing H_2 evolution and promoting selective CO_2 electroreduction to CO at low overpotentials by alloying Au with Pd. *ACS Catal.* **2019,** *9*, 3527-3536.
(74) Gauthier, J. A.; Stenlid, J. H.; Abild-Pedersen, F.; Head-Gordon, M.; Bell, A. T. The Role of Roughening to Enhance Selectivity to C_{2+} Products during CO_2 Electroreduction on Copper. *ACS Energy Lett.* **2021,** *6*, 3252-3260.